Antenna De-Embedding Using Deconvolution With Tikhonov Regularization for mmWave Channel Measurement

Congle Ge, Ruonan Zhang, *Member, IEEE*, Yi Jiang, Lin Cai, *Fellow, IEEE*, and Bin Li, *Member, IEEE*

***Abstract*— Antenna-free channel models can reflect real multipath propagation and can be applied widely for performance analysis, simulation, and physical emulation, combined with specific antennas used in the communication systems. However, the millimeter-wave (mmWave) channel measurement is usually performed by steering horn antennas, and the measured channel responses are actually spatial convolution of the channel propagation models and antenna pattern, which is commonly referred to as the antenna embedding effect. In this work, we propose a novel antenna de-embedding algorithm based on the deconvolution with Tikhonov regularization. By suppressing parts of the observed responses which are disguised by noise, the Tikhonov regularization facilitates the deconvolution of antenna pattern and enables the extraction of propagation models. In particular, in order to minimize the impact of deconvolved noise, we design an optimization algorithm to obtain the appropriate regularization factor with low computational complexity. To validate the proposed approach, we have performed an indoor mmWave channel measurement campaign using two different steering horn antennas. The principal peaks in the synthesized channel responses are accurately reconstructed, and the signal-to-noise ratio (SNR) is improved. The experiments verify that the proposed scheme de-embeds effectively the antenna effect and leads to the antenna-free channel models.**

***Index Terms*— Antenna effect, antenna-free channel model, millimeter wave (mmWave), signal-to-noise ratio (SNR), Tikhonov regularization.**

I. Introduction

THE global bandwidth shortage currently experienced by mobile cellular carriers has largely motivated the exploration of the millimeter-wave (mmWave) frequency spectrum, which is a key enabler for 5G. In [1], the 5G mmWave communication system will offer low-latency high-speed data connection with gigabit speed and high bandwidth. The mmWave channel propagation characteristics are the basis for the development and deployment of antennas and transceivers in typical deployment scenarios. In particular, the space-delay channel model, including the path loss, excess delay, complex gain, and angle-of-arrival/angle-of-departure (AoA/AoD) of the propagation paths [2], is critical to the evaluation and simulation of the candidate transmission systems. The mmWave channel characteristics differ significantly from those below 6 GHz, such as the reflection and diffraction behaviors of the propagation paths [3], [4]. Extensive channel measurements and accurate propagation parameterization are important to establish the space-delay multipath fading model of mmWave channels.

Measurement and modeling mmWave channels have been an active research topic in recent years [5]–[7]. However, different from the traditional channel measurement for sub-6G band, the antenna embedding effect in mmWave channel sounding is an important issue. In order to overcome the large path loss at high frequencies [8]–[15], high-gain and steerable horn antennas are usually employed to capture the spatial channel responses. The captured channel responses actually include the antenna radiation patterns. However, for communication system evaluation, the antenna-free channel model (or propagation model), without the antenna effects on the channel measurement, is needed. Thus, the channel responses for specific communication systems can be reproduced by combining patterns of the specific antennas and the channel propagation model.

It is nontrivial to de-embed the antenna effect in the mmWave measurement where the steering-antenna solution is adopted. On one hand, the captured channel responses are actually the spatial convolution between the antenna-free channel model and the antenna pattern. The deconvolution based on the observed channel responses can be boiled down to an ill-posed problem (or inverse problem) due to the presence of noise. It is not feasible to solve the convolution directly, as simply inversing the antenna pattern may dramatically amplify the involved noise. On the other hand, the measured channel responses can be viewed as the approximation of the real ones, so the ill-posed problem in antenna de-embedding has no exact solution. Therefore, high-accuracy and low-cost method to de-embed the antenna effect from the measurement

Manuscript received 31 January 2021; revised 25 December 2021; accepted 16 April 2022. Date of publication 30 May 2022; date of current version 8 September 2022. This work was supported in part by the National Key Research and Development Program of China under Grant 2020YFB1807003, in part by the National Natural Science Foundation of China under Grant 62171385, in part by the Key Research Program and Industrial Innovation Chain Project of Shaanxi Province under Grant 2019ZDLGY07-10 and Grant 2022ZDLGY05-07, in part by the Natural Science Fundamental Research Program of Shaanxi Province under Grant 2021JM069, and in part by the Natural Sciences and Engineering Research Council (NSERC) of Canada. *(Corresponding author: Ruonan Zhang.)*

Congle Ge, Ruonan Zhang, Yi Jiang, and Bin Li are with the School of Electronic Information, Northwestern Polytechnical University, Xi'an 710072, China (e-mail: bella_mkbz@mail.nwpu.edu.cn; rzhang@nwpu.edu.cn; jiangyiv88@nwpu.edu.cn; libin@nwpu.edu.cn).

Lin Cai is with the Department of Electrical and Computer Engineering, University of Victoria, Victoria, BC V8P 5C2, Canada (e-mail: cai@ece.uvic.ca).

Color versions of one or more figures in this article are available at https://doi.org/10.1109/TAP.2022.3177427.

Digital Object Identifier 10.1109/TAP.2022.3177427

is a challenging and critical issue for mmWave channel measurement and characterization.

To date, a few works have studied this issue. Sun *et al.* [16] introduced how to synthesize omnidirectional path loss, antenna patterns, and received power for adopting directional steering antennas in mmWave channel measurement. This method was demonstrated by the theoretical analysis and an mmWave measurement. In [17], an approach to extracting narrowband channel propagation model was proposed by a de-embedding antenna effect in the spherical vector wave domain (VWD). The channel transfer function reconstructed by de-embedding the mode-to-mode mapping matrix for target antennas was conducted, and the matrix was actually regarded as the channel propagation model in VWD. Käske *et al.* [18] proposed an antenna de-embedding approach by adopting a parameter estimation algorithm (i.e., RIMAX) for the single measurement. This approach based on the effective aperture distribution function (EADF) allows different antennas to be inserted and described. Vinogradov *et al.* [19] introduced a deconvolution method for antenna de-embedding. Due to the existence of the inverse problem, the gross spatial spectrum (GSS) was calculated by an antenna pattern and channel observation, and then, the spatial channel response was synthesized from the selected local maxima spectrum peaks among GSS. This method demonstrated that the reconstructed channel responses with different horn antennas were similar in a field mmWave propagation measurement.

These existing works mainly focused on de-embedding antenna pattern. However, the noise as an inevitable part of channel responses in measurement should be considered, and thus, it may be difficult to obtain the precise propagation model. In addition, a horn antenna is usually rotated with the interval of the antenna half-power beamwidth (HPBW), and thus, the estimation error of path AoA/AoD can reach up to half of the antenna HPBW. As the horn antenna points to a certain angle, it is relatively difficult to discriminate multiple propagation paths, and the pointing angle of the antenna is approximately regarded as the AoA of the single multipath component (MPC). Consequently, the spatial minimum resolution is actually the HPBW and thus is generally low.

In this work, we adopt the spatial sampling scheme: the horn antenna is rotated with a small (i.e., 2°) angular interval, which is much smaller than the HPBW. Thus, this scheme can improve the accuracy of AoA/AoD estimation and deconvolution for channel angular response estimation. Meanwhile, attenuating the impact of noise is also considered as a key factor for antenna de-embedding. Then, based on the spatial sampling scheme for mmWave channel measurements, we design a novel antenna de-embedding algorithm with steering antennas. The main contributions of this article are threefold as follows.

1) Based on the convolutional model of the spatial channel response, a deconvolution method with Tikhonov regularization is proposed to remove the antenna effect. The regularization is actually to perform a filter to minimize the impact of deconvolved noise at the frequencies where the signal-to-noise ratio (SNR) is low. Hence, this approach relieves the illness problem and enables a direct deconvolution solution for the antenna-free channel propagation model in the wave number domain (WND).
2) Since it is crucial to determine the Tikhonov parameter (regularization factor) in the scheme, we design an optimization algorithm to select the appropriate value. Moreover, the computational complexity of this algorithm is low.
3) The proposed approach is verified using mmWave channel measurement data. The measurement was conducted in both the space and frequency domains. We steered two horn antennas with different gains and HPBWs at the receiver (RX) to capture the incoming signals from all azimuth angles. By using the proposed deconvolution method, we obtained the space-frequency channel propagation model. The azimuth/elevation channel response (ACR/ECR), transfer function, and multipath channel impulse response (CIR) were reproduced based on the estimated propagation model.

The rest of this article is outlined as follows. The mmWave channel measurement approach is described in Section II. In Section III, the signal convolutional model in space-frequency domain is defined for mmWave channel measurement. Section IV describes the antenna de-embedding algorithm, and the propagation model construction and channel response synthesis using the estimated propagation model are presented in Section V. In Section VI, we verify that the probing dynamic range and angular resolution can be improved using the simulation. In Section VII, the proposed antenna de-embedding scheme is further verified by a field measurement campaign, and thus, the effectiveness of the proposed algorithm is demonstrated. Section VIII summarizes this article and discusses the future research works.

II. mmWave Channel Measurement Method

In channel measurement, the sounders usually adopt two approaches to realize wideband (or multipath) measurement: direct sequence spread spectrum (DSSS) in the delay domain [20] and sweeping frequency in the frequency domain [21]. The former usually transmits the spread-spectrum signal modulated by pseudo-noise (PN) sequences, and the RX can distinguish the MPCs through the correlation function and directly obtain the multipath CIRs. Furthermore, the propagation parameters of the MPCs, such as excess delay and AoAs, are estimated. The latter is to transmit a single-tone signal, and the carrier frequency increases linearly within the target bandwidth so that the channel frequency response can be obtained through the vector network analyzer (VNA). Then, the multipath CIR is acquired by the inverse Fourier transform (IFT), and MPCs are further extracted and their propagation parameters are estimated. For mmWave channel measurement, due to the high carrier frequency, radio devices are easy to adjust the operating frequency in a large bandwidth, and hence, the sweeping-frequency method is often used.

Considering that the signal received by an omnidirectional antenna is the superposition of MPCs in all directions, steering high-gain horn antennas are widely employed in mmWave

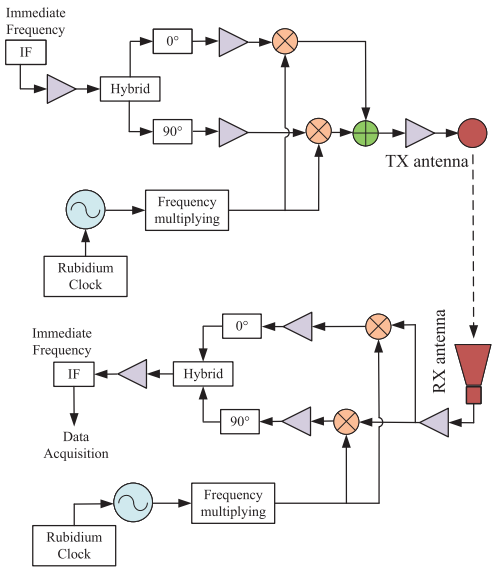

Fig. 1. Block diagram of the channel measurement system.

Fig. 2. High-gain horn antenna equiped with the digital turntable.

channel sounding systems to distinguish the MPCs in the angular domain and meanwhile cope with the large propagation path loss. The block diagram of the typical mmWave channel measurement system is plotted in Fig. 1. At the transmitter (TX) side, the local carrier is produced by frequency multiplying and a high-accuracy rubidium clock, and the in-phase and quadrature components of the intermediate frequency (IF) signal are acquired through phase shift. These two components are upconverted to the mmWave frequency band, then pass through an adder, and radiated by omnidirectional antenna or a directional horn antenna to increase the effective radiation power. At the RX side, the received signal is downconverted to the IF with the same local carrier, and the amplitude and phase of the received signal are calculated according to the in-phase and quadrant components. Thus, the complex channel response at current frequency is obtained. Then, after the frequency sweeping from f_l to f_h, the complex channel transfer function is acquired.

As mentioned in Section I, high-gain horn antennas can increase the received power of the MPCs in mmWave channel measurement. For example, a realistic high-gain horn antenna equipped with the digital turntable is shown in Fig. 2. Due to the small beamwidth, the horn antennas are rotated to

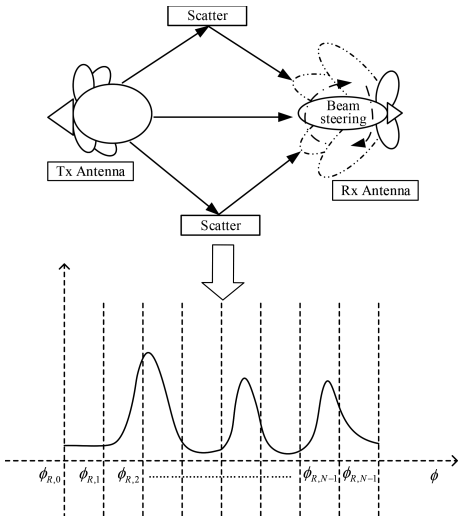

Fig. 3. Spatial channel sampling and steering-antenna measurement.

scan the spatial domain and capture incoming signals in omnidirectional. As shown in Fig. 3, the antenna is steered using the interval of δ in the azimuth domain. The horn antenna may also be rotated vertically to capture the incoming MPCs in the elevation domain. When the sweeping-frequency scheme is employed, the RX antenna points to a certain angle, and the channel is probed at the sweeping frequencies from f_l to f_h. For example, the range of the sweeping frequency is 72.5–73.5 GHz in our verification measurement campaign. Thus, the channel transfer function for every rotation direction is obtained.

III. Channel Model in Space-Frequency Domain Channel Measurement

A. Channel Propagation Model

To describe the wireless signal propagation characteristics and restore the synthesized channel responses free from the impact of different antennas, we are interested in the antenna-free channel propagation model. The channel model, including the frequency and spatial information, can be expressed as

$$h(f,\phi_T,\phi_R)=\sum_{l=1}^{L}h_l(f)\delta\left(\phi_T-\phi_{D,l},\phi_R-\phi_{A,l}\right) \quad (1)$$

where f is the carrier frequency, L is the number of propagation paths, and h_l, $\phi_{A,l}$, and $\phi_{D,l}$ are the antenna-free channel complex gain, AoA, and AoD of the lth path in the azimuth or elevation domain, respectively. In (1), ϕ_T and ϕ_R represent the angle value defined based on the TX and RX antenna coordinates, respectively.

B. Channel Response Using Steering Horn Antenna

The channel sounding using the steering-antenna solution described in Section I is shown in Fig. 3. In practical measurement, the RX antenna points to N directions ($\phi_{R,n}, n = 0, 1, \ldots, N-1$) and the channel is probed at K different

frequencies ($f_k, k = 0, 1, \ldots, K-1$) by discrete sweeping frequency. When the RX antenna points to the direction of $\phi_{R,n}$ and the channel is probed at f_k, the observed complex signal is the combination of the multipath signals from the AoAs ($\phi_{A,l}$ for $l = 0, 2, \ldots, L-1$) that are amplified by antenna complex gains at these angles. As a result, when the RX antenna is rotating, the observed ACRs/ECRs (i.e., the complex signals from the antenna output port) are the spatial convolution of the channel multipath gains and the RX antenna pattern.

For easy presentation and with appropriate generality, we suppose that the TX antenna is omnidirectional. Thus, its pattern can be denoted by $a_T(f, \phi_T) = a_T^o(f)$ (the superscript "o" indicates being omnidirectional). The RX directional antenna pattern is denoted by $a_R(f, \phi_{R,n})$. The observed space-frequency channel response at the direction of $\phi_{R,n}$, denoted by $g(f, \phi_{R,n})$, is hence given by

$$\begin{aligned} g(f, \phi_{R,n}) &= a_T^o(f) h(f, \phi_{R,n}) \otimes a_R(f, \phi_{R,n}) + a_T^o(f) \\ & w_p(\phi_{R,n}) \otimes a_R(f, \phi_{R,n}) + w_s(\phi_{R,n}) \\ &= \int_0^{2\pi} a_T^o(f) h(f, \phi) a_R(f, \phi - \phi_{R,n}) d\phi + w(\phi_{R,n}) \end{aligned} \tag{2}$$

where $w_p(\phi_{R,n})$ is the propagation noise, $w_s(\phi_{R,n})$ represents the system noise, and $w(\phi_{R,n})$ is a mix of them. Note that since the antenna rotation is 2π-periodic, the convolution in (2) is circular.

Thus, we have N discrete samples of the channel spatial response $g(f, \phi_{R,n})$. The measurement results over the rotation angular range and at the frequency f_k is organized in a vector of

$$\mathbf{g}_k^o = [g_{k,0} \quad g_{k,1} \quad \cdots \quad g_{k,N-1}]^{\mathrm{T}} \tag{3}$$

where $g_{k,n}$ (also presented by $g_k[n]$) represents the observed channel response at the rotation direction of $\phi_{R,n}$ and $[\cdot]^{\mathrm{T}}$ represents the transpose. Thus, a total of K omnidirectional channel response vectors are captured at the K frequencies.

The RX antenna pattern is similarly sampled at the direction of $\phi_{R,n}$ for $n = 0, 1, 2, \ldots, N-1$. Thus, the angularly discretized pattern at the frequency of f_k is

$$\mathbf{a}_k = [a_R(f_k, \phi_{R,0}) \quad a_R(f_k, \phi_{R,1}) \quad \cdots \quad a_R(f_k, \phi_{R,N-1})]^{\mathrm{T}}. \tag{4}$$

As the channel is sounded in the space-frequency domain using sweeping-tone signals, consequently, the path excess delay is not directly measured. The omnidirectional discrete spatial channel model of $h(f, \phi_R)$ is

$$\mathbf{h}_k^o = [h_{k,0} \quad h_{k,1} \quad \cdots \quad h_{k,N-1}]^{\mathrm{T}} \tag{5}$$

where $h_{k,n}$ (also denoted by $h_k[n]$) represents the antenna-free channel complex gain at the arrival direction of $\phi_{R,n}$ and frequency of f_k.

The discrete convolution form of the space channel response at a certain frequency f_k is

$$\begin{aligned} g_k[n] &= \left(\mathbf{a}_k \otimes \mathbf{h}_k^o\right)[n] + w[n] \\ &= \sum_{m=0}^{N-1} a_k[m-n|N] h_k[m] + w[n] \end{aligned} \tag{6}$$

where $a_k[m-n|N]$ is that the index takes modulus for N and $w[n]$ represents the discrete form of the noise at the direction of $\phi_{R,n}$. Our purpose is to acquire the antenna-free channel model in the space-frequency domain, $\mathbf{h}_k^o$ in (5), based on the measured channel response $h_k[n]$. The directional CIR in the space-delay domain is acquired through the IFT of the transfer function of the wideband channel response at the direction of $\phi_{R,n}$. Then, we can acquire the multipath propagation parameter set below to obtain the channel model

$$\Omega_p = \{L, h_l, \phi_{A,l}\}, \quad l = 1, 2, \ldots, L. \tag{7}$$

IV. Antenna De-Embedding Algorithm Design and Parameter Estimation

An antenna de-embedding algorithm is introduced for the space-frequency mmWave channel measurement in this section. The algorithm is designed based on the channel response model in (6) where a directional RX steering antenna is adopted. The method can be conveniently extended for adopting directional antennas at TX and RX.

A. Transformation in the WND

We can transform the observed omnidirectional channel angle response in the space domain into the WND by the fast Fourier transform (FFT). Let $\mathbf{G}_k^o = \mathcal{F}(\mathbf{g}_k^o)$, $\mathbf{H}_k^o = \mathcal{F}(\mathbf{h}_k^o)$, $\mathbf{A}_k = \mathcal{F}(\mathbf{a}_k)$, and $\mathbf{W} = \mathcal{F}(\mathbf{w})$ denote the FFT of the channel angular response, propagation model, antenna pattern, and noise, respectively. Thus, (6) can be written in the WND as

$$\mathbf{G}_k^o = \mathcal{F}\left(\mathbf{a}_k \otimes \mathbf{h}_k^o + \mathbf{w}\right) = \mathbf{A}_k \odot \mathbf{H}_k^o + \mathbf{W} \tag{8}$$

where $\odot$ is the Hadamard product. According to (8), the individual component in the matrix computation can be written as

$$G_k^o[n] = A_k[n] H_k^o[n] + W_k[n]. \tag{9}$$

Then, the estimate of the channel complex gain $H_k^o[n]$, denoted by $\hat{H}_k^o[n]$, is

$$\hat{H}_k^o[n] = \begin{cases} \dfrac{G_k^o[n]}{A_k[n]} = H_k^o[n] + \dfrac{W_k[n]}{A_k[n]}, & A_k[n] \neq 0 \\ 0, & A_k[n] = 0. \end{cases} \tag{10}$$

The relative error is defined as the ratio of the absolute error caused by the measurement to the actual value. Generally, the relative error is a better indicator of the reliability of the measurement. The relative error of the solution in (9) is $\|A_k^{-1}[n] W_k[n]\| / \|A_k^{-1}[n] G_k^o[n]\|$, where $\|\cdot\|$ is the Euclidean norm. The relative error of the observation $G_k^o[n]$ is $\|W_k[n]\| / \|G_k^o[n]\|$. The ratio of the two maximum relative

errors is the condition number of $\mathbf{A}_k$, which can be expressed as

$$\mathrm{cond}(\mathbf{A}_k) = \max_{W_k[n]} \frac{\left\| \frac{W_k[n]}{A_k[n]} \right\| \cdot \left\| G_k^o[n] \right\|}{\|W_k[n]\| \cdot \left\| \frac{G_k^o[n]}{A_k[n]} \right\|}. \tag{11}$$

The condition number of matrix $\mathbf{A}_k$ determines the influence of the relative error of the observation on the relative error of the solution in (9). The condition number of the antenna pattern matrix can also be calculated by

$$\mathrm{cond}(\mathbf{A}_k) = \frac{\kappa_{\max}(\mathbf{A}_k)}{\kappa_{\min}(\mathbf{A}_k)} \tag{12}$$

where $\kappa(\cdot)$ represents the singular value of the matrix. For example, the condition number of a 20 dBi horn antenna in our work is 3.7445×10^5. As the condition number of this horn antenna is quite large, it is not possible to perform deconvolution directly by inverting the antenna pattern. This issue is also known as the ill-posed problem.

On the other hand, as shown in (10), the estimate of the channel gain by the antenna pattern inversion (i.e., deconvolution) actually contains two parts: the true propagation gain and the error $((W_k[n])/(A_k[n]))$ caused by noise. The wider the antenna beam is, the more concentrated $A_k[n]$ is. Outside the main beam lobe (in the range of "high frequency" in the WND), the value of $A_k[n]$ can be very small. Consequently, the deconvolution may cause the undesirable "false" peaks.

B. Deconvolution With Tikhonov Regularization

Based on the analysis above, the channel response at the directions where the antenna pattern gain is small should be attenuated. The Tikhonov regularization is an effective approach to solve the ill-posed problem. Therefore, we propose a deconvolution approach based on the Tikhonov regularization to solve the antenna embedding problem for the mmWave channel measurement.

The estimation of the propagation model can be determined in the minimization of

$$\hat{H}_k^o[n] = \arg\min_{\hat{H}_k^o[n]} \left\{ \left\| G_k^o[n] - A_k[n]\hat{H}_k^o[n] \right\|^2 + \lambda \left\| \hat{H}_k^o[n] \right\|^2 \right\} \tag{13}$$

where λ is the regularization factor. In (13), the regularization term $\lambda\|\hat{H}_k^o[n]\|^2$ is included to give preference to solutions with smaller norms. This regularization improves the conditioning of the inverse problem and thus leads to a direct deconvolution solution.

According to (13), a closed-form solution is given by

$$\begin{aligned} \hat{H}_k^o[n] &= \left(\frac{A_k^{\mathrm{H}}[n]}{A_k^{\mathrm{H}}[n]A_k[n] + \lambda} \right) G_k^o[n] \\ &= \left(\frac{\|A_k[n]\|^2}{\|A_k[n]\|^2 + \lambda} \right) \frac{G_k^o[n]}{A_k[n]} \end{aligned} \tag{14}$$

where $[\cdot]^{\mathrm{H}}$ represents the complex conjugate transpose operation. The closed-form solution derivation from (13) to (14) is given in the Appendix.

Before determining the Tikhonov regularization factor, we can further analyze the effect of the regularization item. As we can see, (14) actually performs a filter on the channel observation in the WND, and the filtering weight is

$$F[n] = \frac{\|A_k[n]\|^2}{\|A_k[n]\|^2 + \lambda}. \tag{15}$$

When the antenna has a relatively large gain $\|A_k[n]\|^2 \gg \lambda$, the filter response is $F[n] \approx 1$. On the other hand, when the antenna gain is small ($\|A_k[n]\|^2 \ll \lambda$), the observation is dominated by noise, and we have $F[n] \approx ((\|A_k[n]\|^2)/\lambda)$ such that the noise power is attenuated by $((\|A_k[n]\|^2)/\lambda)$. The Tikhonov regularization allows one to extract the desired propagation model from the observed channel response while discarding the response disguised by noise. Thus, the inverse problem is relieved by utilizing the Tikhonov regularization.

C. Determination of Regularization Factor

It is crucial and nontrivial to properly determine the regularization factor λ for the minimization in (13). Obviously, according to (15), if it is too large, the obtained propagation model will be distorted, but if it is too small, the result will be dominated by the noise from the "high-frequency" components in the WND and tends to exhibit a lot of false spikes. The L-curve method (LCM) [22] and the generalized cross validation (GCV) [23] have been proposed to select the optimal regularization factor, and the two effective methods have been widely used. Both algorithms aim to solve the minimum mean square error (MMSE) between the estimated and measured results.

However, the observed channel responses in field channel measurement contain the extra noise, and thus, it is infeasible to determine the regularization factor by adopting the GCV and LCM in this work. We propose an optimization algorithm to determine the appropriate value of the regulation factor and suppress the involved noise in this section. Given that the designed propagation model in (13) based on the Tikhonov regularization, the idea is to reconstruct the channel angular response through the antenna pattern and estimated channel model, i.e., $A_k[n]\hat{H}_k^o[n]$, and allows the synthesized result to deviate from the observation with the noise power. Therefore, the regularization factor λ should be selected such that the mean square deviation equals the noise power, which is expressed as

$$E\left[\left| G_k^o[n] - A_k[n]\hat{H}_k^o[n] \right|^2 \right] = \sigma_w^2 \tag{16}$$

where $E[\cdot]$ is the expectation and σ_w^2 is the variance of the white noise. The noise power can be estimated from the observed channel response. For the azimuth/elevation angles where the antenna gain $A_k[n]$ is small, the observation is dominated by noise. Hence, the noise power can be approximated by the variance of $G_k^o[n]$ at these directions. As a criterion to decide the range where the noise contribution dominates, we can use the ratio of the magnitude of the antenna pattern at a given frequency to the maximal magnitude. To facilitate

the expression, we note the regularization loss as

$$f_k(\lambda) = \left| \frac{1}{N} \sum_{n=0}^{N-1} \left| G_k^o - A_k[n] \hat{H}_k^o[n](\lambda) \right|^2 - \sigma_w^2 \right|. \quad (17)$$

As $\hat{H}_k^o[n]$ depends on λ as given in (14), according to (16), our purpose is to solve the minimization of (17), which can be expressed as

$$\lambda^* = \arg\min_{\lambda} \ f_k(\lambda). \quad (18)$$

Equation (17) can be regarded as a piecewise function with respect to the regularization factor, and there should be a theoretical root of the equation (i.e., a particular value of λ) that makes this function equal to zero. However, it is difficult to acquire the exact solution to this high-order nonlinear equation. Thus, it is preferable to get the approximate solution, e.g., the Newton–Raphson (NP) method. On the other hand, determining the optimal regulation factor for solving (18) can also be turned into a problem of solving the minimum, e.g., the gradient descent (GD) method and the Nelder–Mead (NM) algorithm. As the analysis above goes, the regularization factor should be set within a rational range in the mmWave channel measurement. Hence, we design a limited-range NM (LRNM) algorithm. As for why the NM algorithm is selected for constraint, it will be discussed in Section VII-E. The specific steps of LRNM are given as follows.

1) Set the maximum iteration number M, the iteration accuracy ε, the arbitrary initialization λ, and the regularization factor range $[\lambda_{\min}, \lambda_{\max}]$.
2) The NM method is to find the minimum of (17), but the regulation factor obtained by adopting this method is not guaranteed to be in the closed interval. Hence, when calculating the objective function, the input λ_i needs to be constrained to

$$\lambda_m = \frac{\lambda_{\max} - \lambda_{\min}}{2} (\cos \lambda_i + 1) + \lambda_{\min}. \quad (19)$$

Then, λ_m is plugged into the objective function in (17). As we can observe that, λ_m is always in the prescribed range for any λ_i in (19). Please note that λ_i is regarded as an angular value in radians to perform the cosine operation.
3) An output λ_o is acquired when the number of iterations steps exceeds M or the iteration update is less than ε, i.e., $\|\lambda_i - \lambda_{i-1}\| < \varepsilon$. Finally, the optimal regulation factor λ^* is obtained by substituting λ_o into (19).

By utilizing the optimal regularization factor as above, the propagation model in the WND, $\hat{H}_k^o$, can be estimated by (14). Then, the propagation model in the space domain is obtained by IFT as

$$\hat{\mathbf{h}}_k^o = \mathcal{F}^{-1}\left[\hat{H}_k^o\right]. \quad (20)$$

D. mmWave Wideband Antenna De-Embedding

As described in Section II, for mmWave wideband channel measurement, the system scans a spectrum band that consists of K carrier frequencies (f_k for $k = 0, 1, \ldots, K-1$). The narrowband antenna de-embedding algorithm above is repeated at each carrier frequency. Thus, a total of K estimated omnidirectional spatial channel models $\hat{\mathbf{h}}_k^o$ can be acquired. The wideband antenna de-embedding algorithm is given in Algorithm 1.

Algorithm 1 Wideband Antenna De-Embedding Algorithm

Input: $y_k^o, a_R(f_k, \phi_{R,n})$, for $k = 0, 1, \ldots, K-1$
Output: $\hat{\mathbf{h}}_k^o$

for $k = 0$ to $K-1$ **do**
  Acquire the angularly discretized pattern $\mathbf{a}_k$ at the frequency of f_k;
  Transform g_k^o and $a_R(f_k, \phi_{R,n})$ by FFT into the WND;
  Calculate σ_w based on the observed omni-directional channel responses as specified in Sec. IV-C;
  Select the optimal value of λ by using the LRNM algorithm;
  Calculate the channel propagation model $\hat{H}_k^o$ by (14);
  Get $\hat{\mathbf{h}}_k^o$ by converting $\hat{H}_k^o$ from WND to the spatial domain by (20);
end for
return $\hat{\mathbf{h}}_k^o$

V. Propagation Model and Channel Response Reconstruction

A. Propagation Model Construction

Based on the space-frequency channel propagation model $\hat{\mathbf{h}}_k^o$ (obtained in Section IV), we can acquire the omnidirectional or a certain directional CIR in the delay domain and the channel transfer function.

1) *Directional Propagation Model:* For a given direction of $\phi_{R,n}$, the complex channel gains are extracted from $\hat{\mathbf{h}}_k^o$ for all observed frequencies of $f_k (k = 0, 1, \ldots, K-1)$. Thus, the directional transfer function is (the superscript "d" means being directional)

$$\hat{\mathbf{h}}_n^{f,d} = [\hat{h}_{0,n} \quad \hat{h}_{1,n} \quad \cdots \quad \hat{h}_{K-1,n}]^{\mathrm{T}} \quad (21)$$

where $\hat{h}_{k,n}$ is the nth element of $\mathbf{h}_k^o$ calculated by (20). The CIR in delay domain at the rotation angle of $\phi_{R,n}$ is acquired such as $\hat{\mathbf{h}}_n^{\tau,d} = \mathcal{F}_s^{-1}(\hat{\mathbf{h}}_n^{f,d})$, where $\mathcal{F}_s^{-1}(\cdot)$ represents the short-time inverse Fourier transform (STIFT). We can adopt a window function, such as the Hamming window [24], in the frequency domain for the STIFT.
2) *Omnidirectional Propagation Model:* The complex channel gain at a certain delay is obtained by selecting the maximal one among N direction gains at the kth delay. The synthesized omnidirectional gain can be denoted as

$$\hat{h}_k^{\tau,o} = \max \ \hat{\mathbf{h}}_n^{\tau,d}, \quad n \in [0, 1, \ldots, N-1] \quad (22)$$

Then, based on the obtained channel gains at K excess delays, the omnidirectional propagation model in delay domain is denoted as

$$\hat{\mathbf{h}}^{\tau,o} = \left[\hat{h}_0^{\tau,o} \quad \hat{h}_1^{\tau,o} \quad \cdots \quad \hat{h}_{K-1}^{\tau,o}\right]^{\mathrm{T}}. \quad (23)$$

B. Channel Response Reconstruction

The omnidirectional observed ACR/ECR at a certain carrier frequency f_k can be acquired by the convolution of antenna pattern and the estimated propagation model, as shown in Fig. 3, which can be written as

$$\hat{\mathbf{g}}_k^o = \hat{\mathbf{h}}_k^o \otimes \mathbf{a}_k. \tag{24}$$

The directional synthesized transfer function, including the antenna effect, can be obtained by combining channel gains of different frequencies at a given direction of $\phi_{R,n}$, which is

$$\hat{\mathbf{g}}_n^{f,d} = [\hat{g}_{0,n} \quad \hat{g}_{1,n} \quad \cdots \quad \hat{g}_{K-1,n}]^{\mathrm{T}} \tag{25}$$

where $\hat{g}_{k,n}$ is the ACR/ECR at the direction of $\phi_{R,n}$ and frequency of f_k, as calculated in (24). Then, the synthesized directional CIR in the delay domain is acquired through the STIFT, i.e., $\hat{\mathbf{g}}_n^{\tau,d} = \mathcal{F}_s^{-1}(\hat{\mathbf{g}}_n^{f,d})$.

The composite omnidirectional channel response at a certain delay is acquired by selecting the maximal one among N directional responses at the kth delay, i.e.,

$$\hat{g}_k^{\tau,o} = \max\ \hat{\mathbf{g}}_n^{\tau,d}, \quad n \in [0, 1, \ldots, N-1]. \tag{26}$$

Then, based on the omnidirectional channel responses of the K excess delay obtained by (26), the omnidirectional CIR in the delay domain is obtained as

$$\hat{\mathbf{g}}^{\tau,o} = \left[\hat{g}_0^{\tau,o} \quad \hat{g}_1^{\tau,o} \quad \cdots \quad \hat{g}_{K-1}^{\tau,o}\right]^{\mathrm{T}}. \tag{27}$$

In summary, the directional and omnidirectional channel responses in the delay/frequency/space domains are recreated based on the obtained antenna-free channel model. When the measurement antenna pattern is used in (24), the synthesized channel responses can be compared with the observations in the field measurement to verify the antenna de-embedding.

VI. Simulation Validation of the Proposed Scheme

In this section, we perform the simulations to validate the effectiveness of the proposed method and evaluate the performance improvement on the estimation of the angular power spectrum. First, we use the 3GPP spatial channel model extension (SCME) to generate the antenna-free azimuth channel impulse response (ACIR). Then, according to (24), we convolute the generated ACIR with the practical antenna pattern with the gain of 20 dBi to obtain a theoretical ACR. Third, based on (6), we add noise manually on the theoretical ACR to generate the synthetic ACR. Thus, we can perform the antenna de-embedding algorithm on the synthetic ACR with noise and estimate the ACIR. Finally, we can reconstruct the ACR with the estimated ACIR and the antenna pattern and compare the reconstructed ACR with the theoretical ACR.

As an example, we generate three ACIRs and set the noise floor as -96 dBm which is similar to the measured one with the 20 dBi antenna. For the noise floor of -96 dBm in Fig. 4, the SNR of the spectral peak at 148° in the synthetic ACR is actually 3 dB and this MPC cannot be distinguished due to the severe noise. For this case, we have performed 500 simulations based on the Monte Carlo method. Because the MPC around 148° cannot be distinguished for the 3 dB SNR due to severe noise and the percentage of identification can be regarded as zero without loss of generality, we have observed that the percentage for correct identification of this MPC is improved by about 30% by using the proposed method. As an illustrative example, a reconstructed ACR based on the correctly identified MPCs is plotted in Fig. 4. In addition, we can find that the SNR of the reconstructed ACRs has been improved.

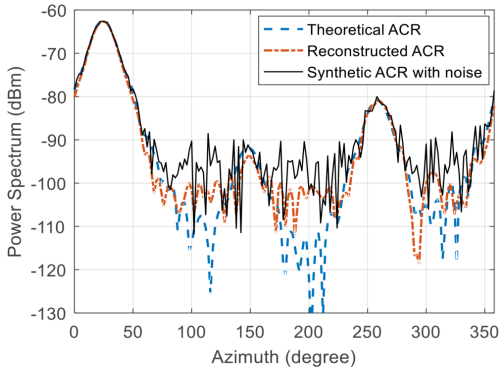

Fig. 4. Theoretical ACR, reconstructed ACR, and synthetic ACR with noise floor of -96 dBm.

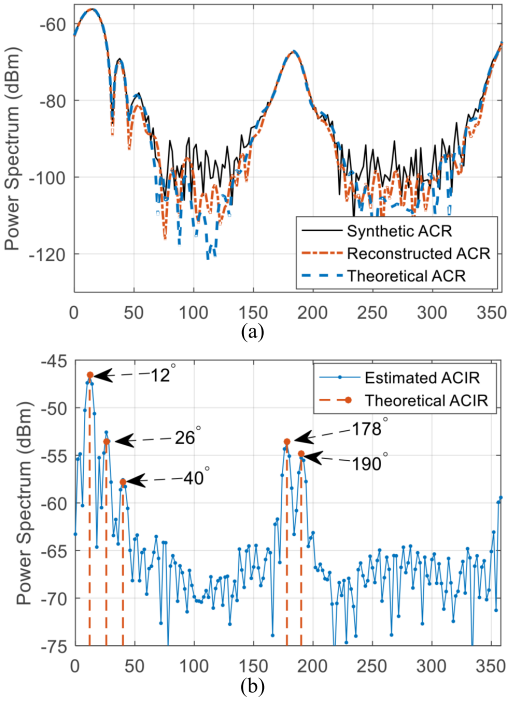

Fig. 5. (a) Theoretical ACR, reconstructed ACR, and synthetic ACR with noise floor of -100 dBm. (b) Theoretical and estimated ACIRs.

On the other hand, to analyze the spatial resolution of MPCs through the deconvolution process, we generate ACIRs with the angular interval of 12° and 14° and use the 20 dBi antenna pattern with the HPBW of 17° in the simulation. In Fig. 5(a), we can find that only one spectral peak appears in the power spectrum of ACR around 184° when the angular interval of the two MPCs is less than the antenna HPBW. We also plot the estimated and theoretical ACIRs in Fig. 5(b). It can be observed that the azimuth angles of the two MPCs

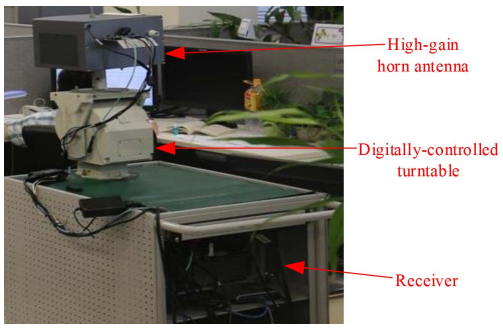

Fig. 6. Channel sounding RX system.

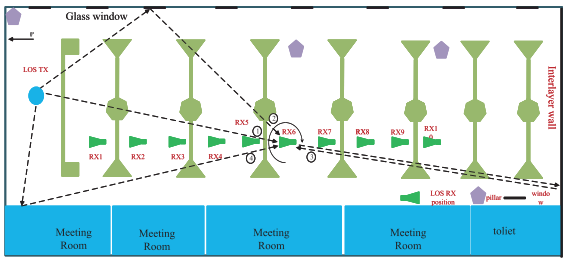

Fig. 7. Office floorplan and measurement positions.

around 184° can be distinguished in the estimated ACIR and are well consistent with those in the theoretical ACIR.

VII. mmWave Channel Measurement and Scheme Validation

A. Performance Metric for Antenna De-Embedding

To verify the proposed approach, we use the correlation coefficient as the metric to evaluate the similarity between the measured and reconstructed ACRs/ECRs. The correlation coefficient at the frequency of f_k, denoted by η, is defined as

$$\eta = \frac{\mathbf{g}_k^o \cdot \hat{\mathbf{g}}_k^{o\mathrm{H}}}{\sqrt{\mathbf{g}_k^o \cdot \mathbf{g}_k^{o\mathrm{H}}} \cdot \sqrt{\hat{\mathbf{g}}_k^o \cdot \hat{\mathbf{g}}_k^{o\mathrm{H}}}} \tag{28}$$

where $\mathbf{g}_k^o$ and $\hat{\mathbf{g}}_k^o$ are the measured and reconstructed omnidirectional ACR/ECR, as given in (3) and (24), respectively.

B. mmWave Channel Measurement Experiment

In order to validate the proposed antenna de-embedding scheme, an mmWave channel measurement campaign was conducted in an indoor office with sweeping frequency from 72.5 to 73.5 GHz. In this whole measurement system, the S-parameter network analyzer at TX was used to generate the target signal, and the RX setting is shown in Fig. 6. The floorplan of the office and the positions of the transceiver are shown in Fig. 7. The size of office was 56 × 34 m^2, and the height of the roof was 4.5 m. The furniture in the office consisted of computers, whiteboard, tables, and so on. One side of the office was a double pane window, and the other sides were the drywall of the conference room. A fixed omnidirectional antenna at TX and two steering horn antennas at RX were adopted. The HPBWs and gains of the two RX antennas were 17°/20 dBi and 6°/30 dBi, respectively.

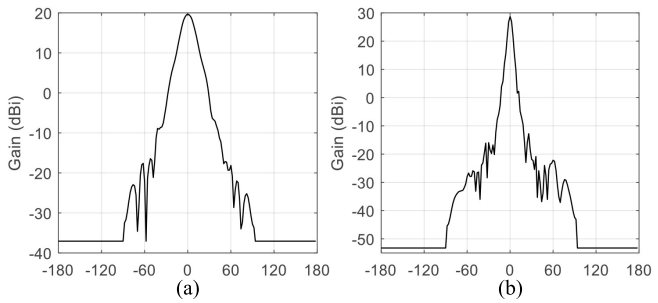

Fig. 8. Antenna pattern. (a) 20 dBi antenna. (b) 30 dBi antenna.

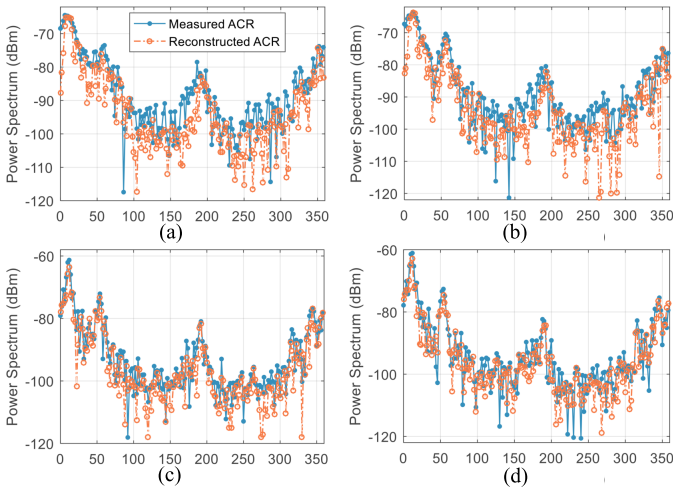

Fig. 9. Reconstructed and measured ACRs with two horn antennas. (a) f_k = 72.572 GHz, 20 dBi antenna. (b) f_k = 72.639 GHz, 20 dBi antenna. (c) f_k = 73.21 GHz, 30 dBi antenna. (d) f_k = 73.34 GHz, 30 dBi antenna.

Their patterns are shown in Fig. 8. The height of the TX side and RX side was 2.4 and 1.5 m, respectively.

During the measurement, the environment was static and no objects moved. The RX antennas were rotated with the 2° interval from 0° to 360° in the horizontal plane. Therefore, at each measured frequency, the complex ACRs with 180 samples were observed.

C. Antenna De-Embedding and ACRs Reconstruction

As illustrative examples, the measured omnidirectional ACRs [$\mathbf{g}_k^o$ defined in (3)] and the reproduced ACRs [$\hat{\mathbf{g}}_k^o$ given in (24)] by adopting 20 and 30 dBi antennas at four different frequencies are shown in Fig. 9. The correlation coefficients between the measured and reconstructed ACRs in Fig. 9 are 0.91, 0.9, 0.95, and 0.96. The azimuth power spectra of the extracted four significant MPCs at the measurement frequencies are plotted in Fig. 10. The AoAs of the four MPCs coincide well with each other. Furthermore, the signal power arriving at the AoAs may differ from each other due to the variation of frequency and measurement errors. According to the AoAs of the four significant MPCs in Fig. 10, the propagation paths are clearly shown in Fig. 7. The first MPC is from the line-of-sight (LOS) propagation path at the AoA of approximately 12°, and therefore, its power is always the largest among the observed MPCs. The reflection of the glass

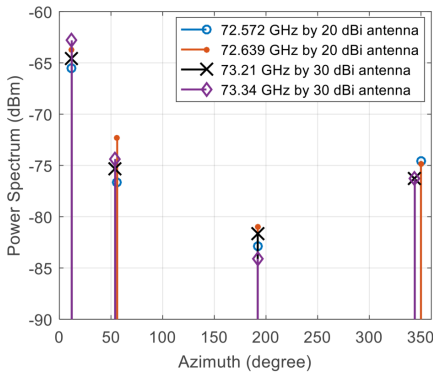

Fig. 10. Azimuth power spectrum of the reconstructed four MPCs using different horn antennas at four frequencies.

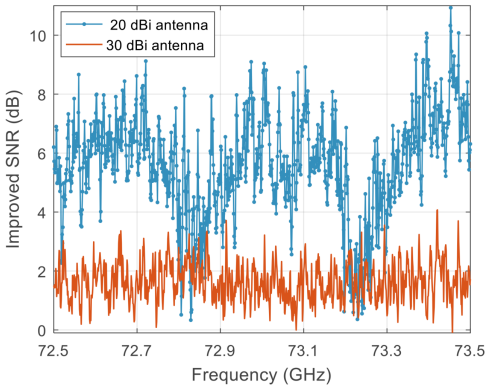

Fig. 11. Improved SNR of the LOS signal in the measured and reconstructed ACRs.

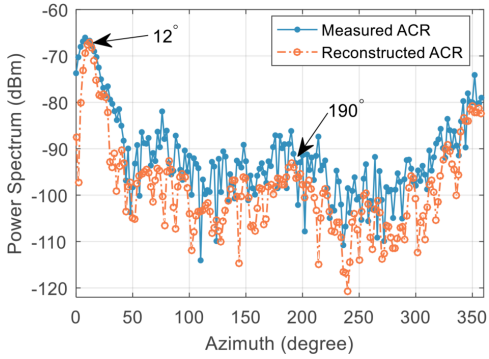

Fig. 12. Measured and reconstructed ACRs by 20 dBi antenna at 73.413 GHz.

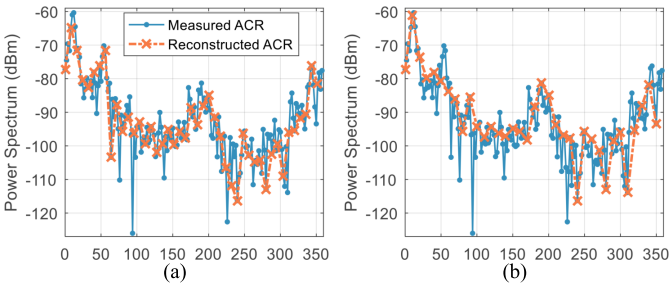

Fig. 13. Measured ACRs, reconstructed ACRs with different rotation steps. (a) $\delta = 8°$. (b) $\delta = 10°$.

window/wall at the top in the floor plan view of the office results in the second path, and it corresponds to the AoA of approximately 56°. Due to the reflection of interlayer wall, the third MPC is probed at the direction of about 192°. The fourth path is caused by the reflection on the wall of the meeting room, and its AoA is around 350°.

The SNRs of the LOS paths in the measured and reconstructed ACRs for the 20 and 30 dBi antenna are denoted by γ_{LOS} and $\hat{\gamma}_{\text{LOS}}$, respectively. Then, the results of SNR improvement, $\hat{\gamma}_{\text{LOS}} - \gamma_{\text{LOS}}$, are plotted for the measurement frequencies in Fig. 11. We can observe that the SNR has been improved at all the measurement frequencies for the 20 dBi antenna, but the SNR improvement is low at about 72.8 and 73.2 GHz. For the purpose to present the performance of the proposed method in terms of SNR improvement, we have done evaluation by both the simulations and measured data. The results show that when the SNR of the received signal is more than about 15 dB, the SNR improvement for the resolved MPCs is about 8 dB on average. For example, for the LoS path at 12° in Fig. 12, the power of the reconstructed LoS path is the same as that of the measured, whereas the noise floor in the reconstructed spectrum has decreased by about 7.6 dB. In this way, we obtain the average SNR improvement of about 8 dB through both the simulations and field measurement data. On the other hand, when the received SNR is below 15 dB, both the estimated signal power and the noise floor reduce, and the SNR improvement decreases to below 8 dB. For example, the power of the reconstructed spectral peak around 190° has decreased by 6 dB in Fig. 12, and the SNR improvement is limited at deep fading bands around 72.8 and 73.2 GHz for the 20 dBi antenna due to the low SNR in Fig. 11 as well. This is as expected because the accuracy of the deconvolution decreases when the channel gains and received SNR are low. In addition, if the noise floor of the measured ACR is close to that of the theoretical ACR, the improvement on the ACR will also be limited. For example, the noise floor of the measured ACRs is about −97 and −102 dBm on average for the 20 and 30 dBi antennas in Fig. 9, respectively, and the LoS path SNR has been improved by about 6 and 1 dB, respectively. As a result, the reconstructed ACRs with the 30 dBi antenna have a small SNR improvement due to the lower noise floor, as shown in Fig. 11.

D. Effect of Steering-Antenna Rotation Interval

The horn antenna rotation step directly determines the precision of the reconstructed ACRs. To study the effect of spatial sampling interval, the observed ACRs with 30 dBi antenna using the rotation steps of $\delta = 8°$ and 10° are extracted from the originally captured signals. Meanwhile, the 30 dBi antenna pattern is similarly sampled with the two designed intervals. After the antenna de-embedding and ACR reconstruction, the measured ACRs with $\delta = 2°$ and the synthetic are shown in Fig. 13. As shown in Fig. 13(a), the peaks of the synthesized ACRs with $\delta = 8°$ deviate from the measured AoAs of MPCs at the azimuth of about 12° and 192°. However, for the sampling setup of $\delta = 10°$ in Fig. 13(b), the multipath at

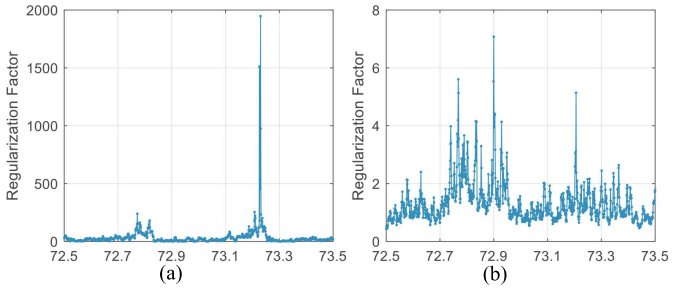

Fig. 14. Obtained regularization factor for different antennas. (a) 20 dBi antenna. (b) 30 dBi antenna.

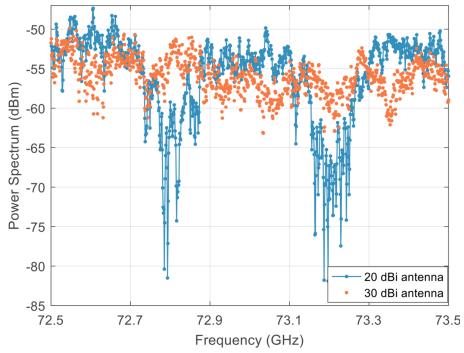

Fig. 15. Measured channel frequency responses with two horn antennas.

the azimuth of around 56° fails to be reconstructed. Therefore, a large rotation angular interval may degrade the estimation of channel propagation model due to the large spatial sampling interval (or the low spatial sampling rate).

A horn antenna is usually installed on a high-precision digitally controlled steerable turntable in an mmWave channel measurement system. As expected and verified by the experiment results, a small rotation angular step is preferable to acquire an antenna-free channel model with a high spatial resolution and reconstruct the channel responses for specific antennas.

E. Determination of the Optimal Regularization Factor

As proposed in Section IV, the regularization factor λ significantly affects the accuracy of the estimated channel propagation models, and hence, how to select the optimal λ is studied by numerical analysis in this section. We first calculate the regularization factor by the NM method in Section IV-C with 20 and 30 dBi antennas. As shown in Fig. 14, λ obtained with 20 dBi antenna is quite large at about 72.8 and 73.2 GHz. To find out the reason of the peaks, the channel frequency responses measured with 20 and 30 dBi antennas are plotted in Fig. 15. We can observe that the frequency response for the 30 dBi antenna is stable, but there are the obvious deep fadings at about 72.8 and 73.2 GHz for the 20 dBi antenna. Therefore, the noise is dominant in the received signals at the two fading frequency bands due to the small channel gains. This is as expected because the regularization factor should be large when the frequency selective fading occurs and the SNR is low. The regularization

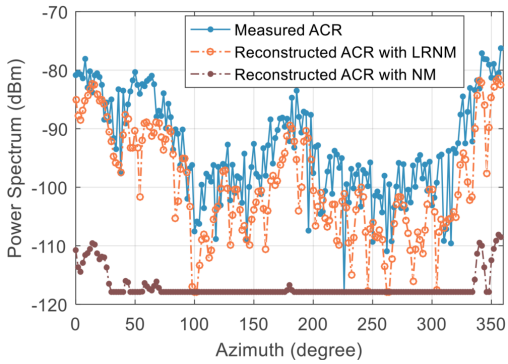

Fig. 16. Measured ACRs, reconstructed ACRs with the NM and LRNM method by 20 dBi antenna at 73.226 GHz.

factor determined by the NM method for 20 dBi antenna is 1510.6 at 73.226 GHz, and the reconstructed ACRs with the NM and LRNM method are plotted in Fig. 16. We can observe that the power of the reconstructed ACR with the NM method is lower than the measured noise floor of about −100 dBm. In such a case, the larger regularization item will not provide reasonable/useful results. This experiment demonstrates why the NM method needs to be constrained. Considering that the regularization factor should be determined for the frequencies without deep fading, the regularization factor range is set between 0.1 and 50.

The regularization loss is used as an evaluation of selecting λ according to (18). Under the same convergence accuracy ($\varepsilon = 10^{-5}$), we calculate the regularization loss obtained by the LRNM, NM, NP, and GD methods with different initial values λ_i and maximum iterations M, for 30 dBi antenna from 72.5 to 72.8 GHz. Compared with Fig. 17(a), the regularization loss calculated by NP increases obviously in Fig. 17(b) due to different λ_i values at some frequencies, but for LRNM, NM, and GD, the regularization loss varies slightly. By comparing Fig. 17(b) and (c), we can observe that the GD method gradually converges with the increase of maximum iterations, resulting in the reduction of regularization loss. However, the regularization loss via NP is still significantly larger than that of LRNM, NM, and GD at some measured frequencies in Fig. 17(c). This is because the NP method fails to converge for the given λ_i of 50. Therefore, more iteration steps are required for the GD method by solving (18). Meanwhile, improper initialization λ_i may cause the divergence of the NP method. The above results show that, compared with the other two methods, the NM and LRNM algorithm can converge with less iteration steps and is not affected by the initialization. Therefore, the NM and LRNM method is more robust and efficient.

To illustrate the convergence of the proposed LRNM algorithm, we plot the convergence curve of the regularization loss and factor with respect to the iteration step M for the channel measurement data at 72.573 GHz with 20 dBi antenna in Fig. 18. It is found that, although different iteration steps are required to achieve convergence, the final convergence value of the regulation factor is basically the same for different initial values of λ_i in Fig. 18(b).

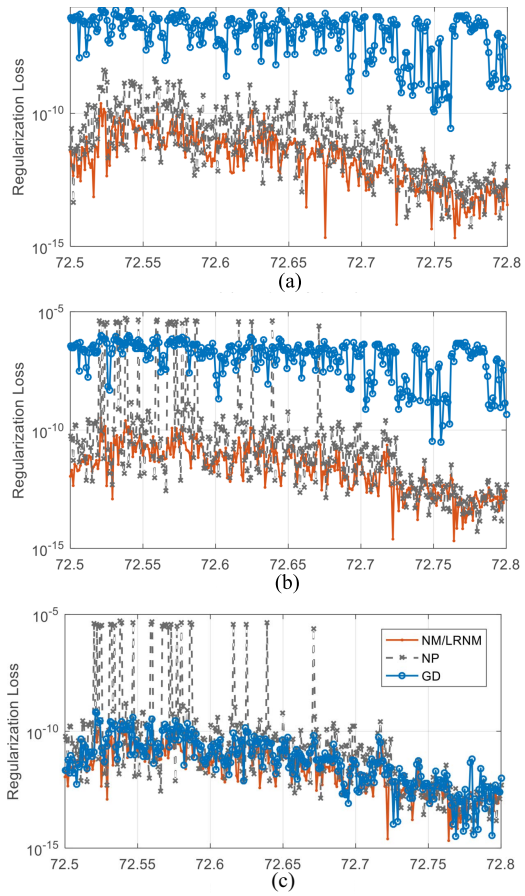

Fig. 17. Calculated regularization loss. (a) $\lambda_i = 45$ and $M = 100$. (b) $\lambda_i = 50$ and $M = 100$. (c) $\lambda_i = 50$ and $M = 1000$.

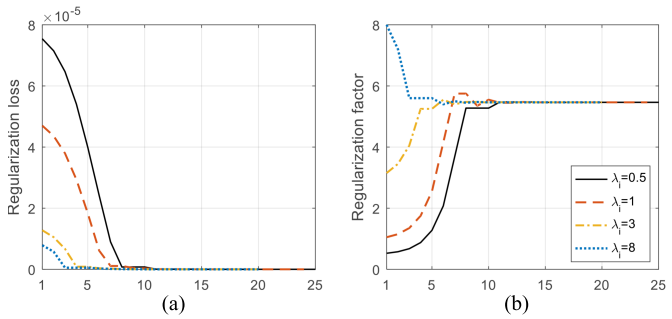

Fig. 18. (a) Regularization loss convergence curve with the varying of iteration step. (b) Regularization factor convergence curve with the varying of iteration step.

F. CIR Reconstruction in Delay Domain

The reconstructed and the measured directional CIRs at the AoAs of 56° and 192° using the 20 and 30 dBi antennas, $\mathbf{g}_n^{\tau,d}$ and $\hat{\mathbf{g}}_n^{\tau,d}$ as defined in Section V-B, are plotted in Fig. 19. As shown in Fig. 19(a), compared with the reconstructed CIRs, the measured CIRs exhibit some false spikes due to the noise.

From Fig. 19, we can observe that the reconstructed directional CIRs using 20 and 30 dBi antennas are very similar at the azimuth angle of 56°. This is also true for the reconstructed CIRs at the azimuth angle of 192°, as shown in Fig. 19(b). Meanwhile, the measured and reconstructed multipath excess

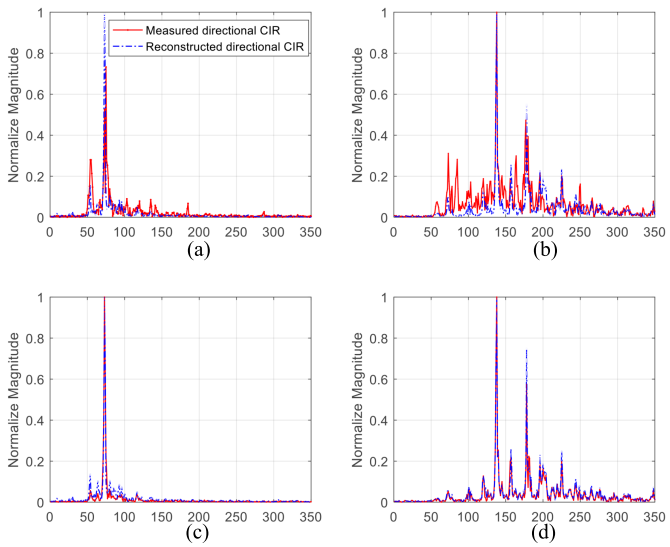

Fig. 19. Measured and reconstructed directional CIRs. (a) AoA = 56°, 20 dBi antenna. (b) AoA = 192°, 20 dBi antenna. (c) AoA = 56°, 30 dBi antenna. (d) AoA = 192°, 30 dBi antenna.

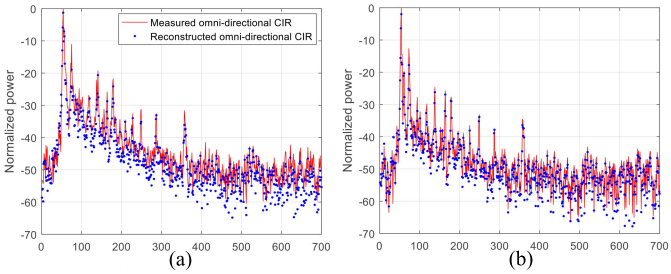

Fig. 20. Measured and reconstructed omnidirectional CIRs. (a) 20 dBi antenna. (b) 30 dBi antenna.

delay at the azimuth angle of 56° is always smaller than that at the azimuth angle of 192°, which actually conforms to the real-world propagation paths, as shown in Fig. 7.

Finally, the reconstructed and the measured omnidirectional multipath CIR using the 20 and 30 dBi antennas in the delay domain, $\mathbf{g}_n^{\tau,o}$ and $\hat{\mathbf{g}}_n^{\tau,o}$, are plotted in Fig. 20. As shown in Fig. 20, it is observed that the reconstructed omnidirectional CIRs have a smaller noise floor compared with the measured ones for both the 20 and 30 dBi antenna, and the trend of SNR improvement is basically the same as that observed in the angular domain.

VIII. Conclusion

It is critical and challenging to perform antenna de-embedding for the mmWave field measurement data because of the inverse problem. This article presented an antenna de-embedding algorithm using deconvolution with Tikhonov regularization for the spatial scanning measurement of mmWave channel. We design an optimization algorithm to select the proper regularization factor and extract the multipath propagation model. The proposed antenna de-embedding method was validated via an mmWave measurement campaign in an office with different steerable antennas. The channel responses are accurately reproduced with the obtained

$$\begin{aligned}\frac{\partial F_k^o[n]}{\partial \hat{H}_k^o[n]} &= \frac{\partial\Big(\big(G_k^o[n]-A_k[n]\hat{H}_k^o[n]\big)^{\mathrm{H}}\big(G_k^o[n]-A_k[n]\hat{H}_k^o[n]\big)\Big)}{\partial \hat{H}_k^o[n]}+\frac{\partial\big(\lambda \hat{H}_k^{o\mathrm{H}}[n]\hat{H}_k^o[n]\big)}{\partial \hat{H}_k^o[n]}\\ &= \frac{\partial\big(G_k^{o\mathrm{H}}[n]G_k^o[n]-G_k^{o\mathrm{H}}[n]A_k[n]\hat{H}_k^o[n]-\hat{H}_k^{o\mathrm{H}}[n]A_k^{\mathrm{H}}[n]G_k^o[n]\big)}{\partial \hat{H}_k^o[n]}+\frac{\partial\big(\hat{H}_k^{o\mathrm{H}}[n]A_k^{\mathrm{H}}[n]A_k[n]\hat{H}_k^o[n]+\lambda\hat{H}_k^{o\mathrm{H}}[n]\hat{H}_k^o[n]\big)}{\partial \hat{H}_k^o[n]}\\ &= -A_k^{\mathrm{T}}[n]G_k^{o*}[n]+A_k^{\mathrm{T}}[n]A_k^{*}[n]\hat{H}_k^{o*}[n]+\lambda\hat{H}_k^{o*}[n] \qquad (30)\end{aligned}$$

antenna-free propagation model in the delay/frequency/space domains. It is shown that the proposed method effectively de-embeds antenna effect and attenuates the impact of the noise inherent in the deconvolution. Furthermore, with the same accuracy condition, the experimental results indicate that the proposed LRNM algorithm is robust and efficient for various initial values. Our proposed antenna deconvolution method can also be applied in communication systems to perform channel estimation, for example, to obtain the multipath CIRs. In future works, we will further verify the consistence among the antenna-free propagation models estimated by different antennas. Predicting channel characteristics and models based on available propagation profiles in different frequency bands is also an interesting research topic.

APPENDIX
DERIVATION OF ANTENNA-FREE CHANNEL MODEL IN (14)

As described in Section IV, the antenna-free channel model can be solved by (13). Formula (13) can be rewritten as

$$F_k^o[n]=\left\|G_k^o[n]-A_k[n]\hat{H}_k^o[n]\right\|^2+\lambda\left\|\hat{H}_k^o[n]\right\|^2. \qquad (29)$$

In order to minimize (13), the partial derivative of (29) with respect to $\hat{H}_k^o[n]$ can be expressed as (30), as shown at the top of the page, where $[\cdot]^*$ is the complex conjugate operation.

Then, let the partial derivative of (29) be zero, which can be expressed as

$$-A_k^{\mathrm{T}}[n]G_k^{o*}[n]+A_k^{\mathrm{T}}[n]A_k^{*}[n]\hat{H}_k^{o*}[n]+\lambda\hat{H}_k^{o*}[n]=0. \qquad (31)$$

From (31), we can further deduce

$$\hat{H}_k^o[n]=\left(A_k^{\mathrm{H}}[n]A_k[n]+\lambda\right)^{-1}A_k^{\mathrm{H}}[n]G_k^o[n]. \qquad (32)$$

Finally, we can obtain the propagation model as shown in (32).

REFERENCES

[1] R. Ford, M. Zhang, M. Mezzavilla, S. Dutta, S. Rangan, and M. Zorzi, "Achieving ultra-low latency in 5G millimeter wave cellular networks," *IEEE Commun. Mag.*, vol. 55, no. 3, pp. 196–203, Mar. 2017.

[2] R. Zhang *et al.*, "Two-dimensional DoA estimation for multipath propagation characterization using the array response of PN-sequences," *IEEE Trans. Wireless Commun.*, vol. 15, no. 1, pp. 341–356, Jan. 2016.

[3] J. Ko *et al.*, "Millimeter-wave channel measurements and analysis for statistical spatial channel model in in-building and urban environments at 28 GHz," *IEEE Trans. Wireless Commun.*, vol. 16, no. 9, pp. 5853–5868, Sep. 2017.

[4] Aalto University, BUPT, CMCC, Nokia, NTT DOCOMO, New York University, Ericsson, Qualcomm, Huawei, Samsung, Intel, University of Bristol, KT Corporation, and University of Southern California, "5G channel model for bands up to 100 GHz," Tech. Rep., Dec. 2015. [Online]. Available: http:// www.5gworkshops.com/5GCM.html

[5] M. K. Samimi and T. S. Rappaport, "3-D millimeter-wave statistical channel model for 5G wireless system design," *IEEE Trans. Microw. Theory Techn.*, vol. 64, no. 7, pp. 2207–2225, Jul. 2016.

[6] N. Iqbal *et al.*, "Multipath cluster fading statistics and modeling in millimeter-wave radio channels," *IEEE Trans. Antennas Propag.*, vol. 67, no. 4, pp. 2622–2632, Apr. 2019.

[7] X. Wu *et al.*, "60-GHz millimeter-wave channel measurements and modeling for indoor office environments," *IEEE Trans. Antennas Propag.*, vol. 65, no. 4, pp. 1912–1924, Apr. 2017.

[8] D. Chizhik, J. Du, R. Feick, M. Rodriguez, G. Castro, and R. A. Valenzuela, "Path loss and directional gain measurements at 28 GHz for non-line-of-sight coverage of indoors with corridors," *IEEE Trans. Antennas Propag.*, vol. 68, no. 6, pp. 4820–4830, Jun. 2020.

[9] A. Valcarce, G. D. L. Roche, L. Nagy, J. F. Wagen, and J. M. Gorce, "A new trend in propagation prediction," *IEEE Veh. Technol. Mag.*, vol. 6, no. 2, pp. 73–81, Jun. 2011.

[10] X. Yin, C. Ling, and M.-D. Kim, "Experimental multipath-cluster characteristics of 28-GHz propagation channel," *IEEE Access*, vol. 3, pp. 3138–3150, 2015.

[11] G. R. MacCartney, J. Zhang, S. Nie, and T. S. Rappaport, "Path loss models for 5G millimeter wave propagation channels in urban microcells," in *Proc. IEEE Global Commun. Conf. (GLOBECOM)*, Atlanta, GA, USA, Dec. 2013, pp. 3948–3953.

[12] N. Zhang, X. Yin, S. X. Lu, M. Du, and X. Cai, "Measurement-based angular characterization for 72 GHz propagation channels in indoor environments," in *Proc. IEEE Globecom Workshops (GC Wkshps)*, Dec. 2014, pp. 370–376.

[13] M. Samimi *et al.*, "28 GHz angle of arrival and angle of departure analysis for outdoor cellular communications using steerable beam antennas in New York City," in *Proc. IEEE 77th Veh. Technol. Conf. (VTC Spring)*, Dresden, Germany, Jun. 2013, pp. 1–6.

[14] M. K. Samimi, G. R. MacCartney, S. Sun, and T. S. Rappaport, "28 GHz millimeter-wave ultrawideband small-scale fading models in wireless channels," in *Proc. IEEE 83rd Veh. Technol. Conf. (VTC Spring)*, May 2016, pp. 1–6.

[15] T. S. Rappaport *et al.*, "Broadband millimeter-wave propagation measurements and models using adaptive-beam antennas for outdoor urban cellular communications," *IEEE Trans. Antennas Propag.*, vol. 61, no. 4, pp. 1850–1859, Apr. 2013.

[16] S. Sun, G. R. MacCartney, M. K. Samimi, and T. S. Rappaport, "Synthesizing omnidirectional antenna patterns, received power and path loss from directional antennas for 5G millimeter-wave communications," in *Proc. IEEE Global Commun. Conf. (GLOBECOM)*, Dec. 2014, pp. 1–7.

[17] Y. Miao, K. Haneda, M. Kim, and J.-I. Takada, "Antenna de-embedding of radio propagation channel with truncated modes in the spherical vector wave domain," *IEEE Trans. Antennas Propag.*, vol. 63, no. 9, pp. 4100–4110, Sep. 2015.

[18] M. Käske, C. Schneider, W. Kotterman, and R. Thomä, "Solving the problem of choosing the right MIMO measurement antenna: Embedding/de-embedding," in *Proc. 5th EUCAP*, Rome, Italy, Apr. 2011, pp. 2551–2555.

[19] R. Zhang, Y. Zhou, X. Lu, C. Cao, and Q. Guo, "Antenna deembedding for mmwave propagation modeling and field measurement validation at 73 GHz," *IEEE Trans. Microw. Theory Techn.*, vol. 65, no. 10, pp. 3648–3659, Oct. 2017.

[20] E. Vinogradov, A. Bamba, W. Joseph, and C. Oestges, "Physical-statistical modeling of dynamic indoor power delay profiles," *IEEE Trans. Wireless Commun.*, vol. 16, no. 10, pp. 6493–6502, Oct. 2017.

[21] K. Saito, J.-I. Takada, and M. Kim, "Dense multipath component characteristics in 11-GHz-band indoor environments," *IEEE Trans. Antennas Propag.*, vol. 65, no. 9, pp. 4780–4789, Sep. 2017.

[22] P. C. Hansen, "Analysis of discrete ill-posed problems by means of the L-curve," *SIAM Rev.*, vol. 34, no. 4, pp. 561–580, Dec. 1992.

[23] G. H. Golub, M. Heath, and G. Wahba, "Generalized cross-validation as a method for choosing a good ridge parameter," *Technometrics*, vol. 21, no. 2, pp. 215–223, May 1979.
[24] J. Karedal, S. Wyne, P. Almers, F. Tufvesson, and A. F. Molisch, "A measurement-based statistical model for industrial ultra-wideband channels," *IEEE Trans. Wireless Commun.*, vol. 6, no. 8, pp. 3028–3037, Aug. 2007.

Congle Ge received the B.E. degree in measurement and control technology and instrument from North Minzu University, Yinchuan, China, in 2017, and the M.Sc. degree in electronic and communication engineering from Ningxia University, Yinchuan, in 2019. He is currently pursuing the Ph.D. degree in information and communication engineering with Northwestern Polytechnical University, Xi'an, China.

His research interests include unmanned aerial vehicle (UAV) channel measurement and modeling, MIMO channel, and channel parameter estimation.

Ruonan Zhang (Member, IEEE) received the B.S. and M.Sc. degrees from Xi'an Jiaotong University, Xi'an, China, in 2000 and 2003, respectively, and the Ph.D. degree from the University of Victoria, Victoria, BC, Canada, in 2010, all in electrical and electronics engineering.

He was an IC Design Engineer with Motorola, Inc., Tianjin, China, and Freescale Semiconductor, Inc., Tianjin, from 2003 to 2006. Since 2010, he has been with the Department of Communication Engineering, Northwestern Polytechnical University, Xi'an, where he is currently a Professor. His research interests include wireless channel measurement and modeling, architecture and protocol design of wireless networks, and satellite communications.

Dr. Zhang was a recipient of the New Century Excellent Talent Grant from the Ministry of Education of China. He served as a Local Arrangement Co-Chair for the IEEE/CIC International Conference on Communications in China (ICCC) in 2013, the Industry Track and Workshop Chair for the IEEE International Conference on High Performance Switching and Routing (HPSR) in 2019, and an Associate Editor for the *Journal of Communications and Networks*.

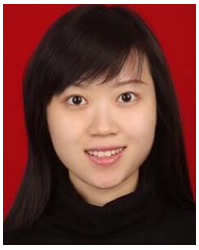

Yi Jiang received the B.S., M.Sc., and Ph.D. degrees in communication and information system from Northwestern Polytechnical University, Xi'an, China, in 2002, 2005, and 2008, respectively.

Since 2005, she has been with the Department of Communication Engineering, Northwestern Polytechnical University, where she is currently an Associate Professor. Her current research interests include the Internet of Things, wireless sensor networks, RFID systems, and wireless channel measurement and modeling.

Lin Cai (Fellow, IEEE) received the M.A.Sc. and Ph.D. degrees (awarded Outstanding Achievement in Graduate Studies) in electrical and computer engineering from the University of Waterloo, Waterloo, ON, Canada, in 2002 and 2005, respectively.

Since 2005, she has been with the Department of Electrical and Computer Engineering, University of Victoria, Victoria, BC, Canada, where she is currently a Professor. Her research interests span several areas in communications and networking, with a focus on network protocol and architecture design supporting emerging multimedia traffic and the Internet of Things.

Dr. Cai is an NSERC E.W.R. Steacie Memorial Fellow and a fellow of the Engineering Institute of Canada (EIC). In 2020, she was elected as a member of the Royal Society of Canada's College of New Scholars, Artists and Scientists, and the 2020 "Star in Computer Networking and Communications" by N2Women. She has co-founded and chaired the IEEE Victoria Section Vehicular Technology and Communications Joint Societies Chapter. She has been elected to serve the IEEE Vehicular Technology Society Board of Governors from 2019 to 2024. She has served as the Associate Editor-in-Chief for IEEE TRANSACTIONS ON VEHICULAR TECHNOLOGY, a member of the Steering Committee of the IEEE TRANSACTIONS ON BIG DATA (TBD) and IEEE TRANSACTIONS ON CLOUD COMPUTING (TCC), an Associate Editor of the IEEE INTERNET OF THINGS JOURNAL, IEEE/ACM TRANSACTIONS ON NETWORKING, IEEE TRANSACTIONS ON WIRELESS COMMUNICATIONS, IEEE TRANSACTIONS ON VEHICULAR TECHNOLOGY, IEEE TRANSACTIONS ON COMMUNICATIONS, *EURASIP Journal on Wireless Communications and Networking*, *International Journal of Sensor Networks*, and *Journal of Communications and Networks* (JCN), and a Distinguished Lecturer of the IEEE VTS and ComSoc Societies.

Bin Li (Member, IEEE) received the B.S. and Ph.D. degrees in electrical and electronics engineering from Xi'an Jiaotong University, Xi'an, China, in 2006 and 2014, respectively.

Since 2014, he has been with the Department of Communication Engineering, Northwestern Polytechnical University, Xi'an, where he is currently an Associate Professor. His current research interests include the Internet of Things, network coding, MIMO, and wireless channel measurement modeling.